GISCIENCE & REMOTE SENSING
2022, VOL. 59, NO. 1, 1406–1425
https://doi.org/10.1080/15481603.2022.2118430

Taylor & Francis
Taylor & Francis Group

Multitemporal impervious surface estimation via an optimized stable/change pixel detection approach

Wei Fan [a,b], Jinsong Chen [c,d], Xiaoli Li [c,d], Paolo Tarolli [e] and Jin Wang [a,c]

[a]Beidou Research Institute, Faculty of Engineering, South China Normal University, Foshan, China; [b]Department of Geography, University of Wisconsin-Milwaukee, Milwaukee, WI, USA; [c]Shenzhen Institutes of Advanced Technology, Chinese Academy of Sciences, Shenzhen, China; [d]Shenzhen Engineering Laboratory of Ocean Environmental Big Data Analysis and Application, Shenzhen, China; [e]Department of Land, Environment, Agriculture and Forestry, University of Padova, Legnaro (PD), Italy

ABSTRACT

Remote sensing techniques have proved its efficacy for the impervious surface mapping, which is a significant indicator of urbanization process and environmental status. However, systematic and random errors in the existing methods still impact the reliability of subpixel impervious surface estimation, generating compounded errors when conducting multitemporal monitoring. The compounded errors of the conventional methods often significantly impact the temporal consistency of the results. In this study, a novel method based on a straightforward pixel change detection approach was put forward to improve the estimation of multitemporal impervious surface area. Two experimental areas located in Rome in Italy and Shenzhen in China were chosen to testify the generality of the proposed method to estimate different types of impervious surfaces worldwide. By reducing the compounded errors, the proposed method demonstrated its efficiency in achieving higher accuracy in both study areas without involving extensive data sources and intensive manual tasks. Compared with the conventional classification and regression tree algorithm, the overall mean average error and root mean square error of this study declined by more than 15.55% and 8.63%, respectively, and R^2 increased from approximately 0.93 to 0.96. The proposed method also drastically reduced the standard deviation of the multitemporal percent ISA of the stable pixels. The accurate change estimation of percent ISA has been a fundamental but challenging issue associated with monitoring and understanding the urban environment. Therefore, our proposed method, with its improved ability to estimate impervious surface change both spatially and temporally, can provide accurate information required for urban environment research.

ARTICLE HISTORY
Received 27 April 2022
Accepted 17 August 2022

KEYWORDS
Impervious surface; change detection; classification and regression tree; remote sensing

1 Introduction

Rapid population growth has occurred in urban areas globally. Since the 1990s, the worldwide urban population has increased from 2.3 billion or 43% of the total global population to 4.4 billion (56.2%). This number is predicted to reach 60% by 2030 (UNHabitat 2020, 2016). The concentration of a massive population in urban areas inevitably leads to urban expansion, which greatly influences the environment in urban areas (Jiaqiang et al. 2019; Limin et al. 2003; Huidong et al. 2022). However, monitoring urban expansion is challenging due to the heterogeneous distribution of the urban landscape, especially when compared with natural areas (Duran, Musaoglu, and Seker 2006; Wu 2004; Stow and Chen 2002). Traditional pixel-level remote sensing methods are insufficient for monitoring environmental change in rapidly urbanizing areas (Ridd 1995; Weng 2012).

Impervious surface is an indicator that can quantitively measure the urbanization impacts. As a key environmental indicator, it presents a unique perspective for measuring urbanization and its effects (Arnold and James Gibbons 1996). Impervious surface refers to material that cannot be infiltrated by water. In urban areas, it is mainly comprised of anthropogenic elements, including building roofs, parking lots, and drive/walk ways. The urban environment can be strongly impacted by the intensification of impervious surfaces in many ways, such as vegetation reduction (Phinn et al. 2002; Dipanwita et al. 2021), waterlogging (Dams et al. 2013; Huafei et al. 2018), water quality degradation (Schueler 1994; Luo et al. 2018; Salerno, Gaetano, and Gianni 2018), and the heat island effect (Mathew, Khandelwal, and Kaul 2016; Yuan and Bauer 2007; Sekertekin and Zadbagher 2021).

CONTACT Jin Wang egmontwj@gmail.com

This article has been corrected with minor changes. These changes do not impact the academic content of the article.

Urban environmental research now requires higher efficiency and accuracy of impervious surface estimation. Ground measurement approaches, such as GPS based field survey, are time-consuming and costly (Weng 2012). Hence, the remote sensing technique has rapidly gained prominence in impervious surface studies since the 2000s because of its ability to cover more areas at lower financial costs (Bauer et al. 2004; Weng 2012; Sinha, Santra, and Santra Mitra 2020). Per-pixel methods, such as post-classification process (Dougherty et al. 2004), remote sensing indicator (Piyoosh and Ghosh 2017; Wang and Mingshi 2021), imagery transformation (Cablk and Minor 2003), and classification decision tree algorithm (Zhang, Zhang, and Lin 2014), have been developed and applied for mapping impervious surfaces. However, because of the coarse spatial resolution and high heterogeneity of urban landscape, the pixels of the low/medium remote sensing imagery (>30 m) are greatly mixed with multiple landcover types (Chen et al. 2021), usually with significant impacts on the per-pixel method accuracy (Dengsheng, Moran, and Hetrick 2011; Limin et al. 2003). Although high-resolution imagery can drastically reduce the mixing problems, data accessibility is limited, especially for multitemporal monitoring over an extended period (Huang et al. 2021; Hsieh, Lee, and Yu Chen 2001). Alternatively, easily accessed medium-resolution imagery, such as the Sentinel and Landsat series, have already formed long-term observations of the earth surface. In order to overcome the mixed pixel problem, subpixel methods have been continuously developed and improved to estimate the percent ISA using medium-resolution imageries (Dengsheng, Moran, and Hetrick 2011).

Compared with other conventionally used subpixel methods, such as linear spectral mixture analysis (Ridd 1995) or linear regression (Shao and Liu 2014), the classification and regression tree (CART) is capable of estimating the non-linear relationship between the independents and target variables (Yang et al. 2003). The CART algorithm can estimate percent ISA through a rule-based model that continuously separates each parent node into two child nodes, which are regarded as potential parent nodes for the next separation (Breiman et al. 1984). The rule-based algorithm for predicting target variables is recursively modified according to sample data. Huang and Townshend (2003) made significant advancements by replacing the single target variable with a linear regression model for each subset, enabling the CART algorithm to predict continuous variables. This improvement was based on a reasonable assumption: while a single linear model may not be applicable to the entire dataset, it can be suitable for each sub-dataset with normal distributions and low intraclass differences, which are well classified by Breiman's algorithm. Yang et al. (2003) obtained sample impervious surface data by overlapping the high-resolution imagery to grids with a resolution of 30 m, and calculated percent ISA using the CART algorithm. It is frequently modeled by using plots of finer resolution imageries for producing sample and validation data, and coarser resolution imageries for estimating the percent ISA of one city or metropolitan area. CART has been further employed by Xian and Crane (2005), Yang et al. (2009), Jungho et al. (2012), and Cao et al. (2019) to estimate percent ISA based on various sets of medium-resolution imagery. The US National Land Cover Database (NLCD) has applied CART as the primary method for estimating impervious surface area since 2006 (Xian and Homer 2010). Being capable of estimating the non-linear relationship between independent and target variables, CART is thought to outperform linear regression models with higher prediction accuracy (Yang et al. 2003; Wang et al. 2018).

However, the compounded error remains a major problem of multitemporal impervious surface estimation using conventional subpixel methods, including CART (Deng and Zhu 2020). Compounded error is accumulated by each phase's errors from the change detection (Pilon 1988). Previous studies noted that for both the pixel-based and subpixel method, each phase's systematic and random errors were often compounded in the final multitemporal results (Lamar, McGraw, and Warner 2005; Zhu 2017). The false temporal variation which disagrees with the actual earth surface change process can be frequently observed in previous studies, even those using a high-precision subpixel model (Dengsheng, Moran, and Hetrick 2011; Powell et al. 2007; Wu et al. 2017; Yao et al. 2020). Additionally, previous studies on impervious surface change are often conducted with temporal intervals of five or more years, which are insufficient to detect the earth surface's temporary but remarkable change during rapid urbanization processes, such as construction sites and temporary

vegetation (Liu et al. 2019). It is also infeasible to define the exact time the permanent change occurs with a relatively long temporal interval. Therefore, Zhu (2017) suggested that conventional subpixel methods were generally not suitable for change detection. Researchers have reduced the temporal inconsistency problem in recent pilot studies using a continuous change detection (CCD) model (Deng and Zhu 2020; Liu et al. 2019). However, a CCD model requires dense stacks of multitemporal cloud-free imageries, which are often not available in many humid regions, such as the subtropical humid monsoon zone. The imaging conditions of these regions are often inadequate to produce the required seasonal imagery datasets.

This study proposes a novel method to improve multitemporal ISA estimation in an attempt to solve the aforementioned problems. Based on straightforward remote sensing change detection in order to reduce multitemporal inconsistency, the estimation of percent ISA is improved both spatially and temporally. The proposed method is objective, reliable, and reproducible without extensive data sources and intensive manual tasks. The proposed method also aiming to accurately estimate multitemporal percent ISA in areas with limited access to cloud-free imageries, and further generate reliable basic data for environmental research on urban planning, microclimate, water cycle, and other relevant issues.

2 Materials and methods

2.1 Study area

In this study, by selecting the two experimental areas located in Rome, Italy and Shenzhen, China, the generality of the proposed method to estimate multitemporal impervious surfaces worldwide was validated (Figure 1). Each area covered 225 km^2 and encompassed the intensely developed urban area of the city centers. Rome and Shenzhen are among the largest cities in the European Union and China, respectively. The population of Rome at the time of this study was 4.2 million, and Shenzhen was 18 million (ISTAT, Italian National Institute of Statistics 2021; Shenzhen Statistics Bureau 2021). A diversity of impervious surfaces were distributed throughout the study areas, from modern skyscrapers to historical building complexes over three thousand years old. Shenzhen has been under a rapid urbanization process over the last

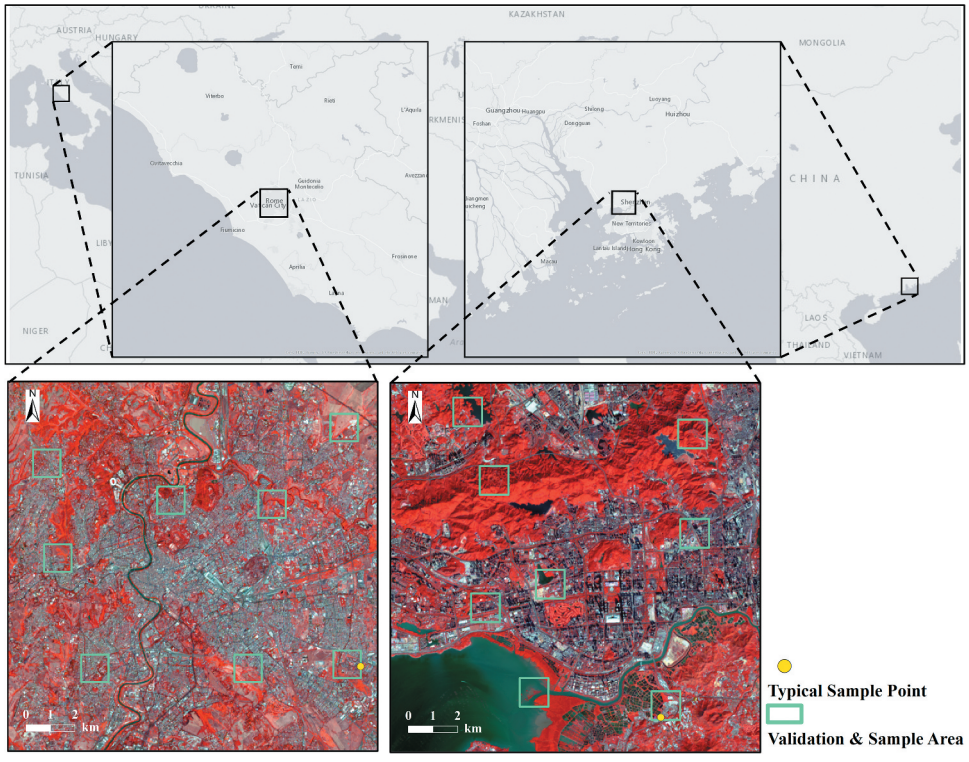

Figure 1. Location of the study areas in Rome (Italy) and Shenzhen (China). Landsat 8 OLI imageries of 2021 are color infrared composited and displayed together with a typical sample point and validation and sample area.

ten years, while Rome has remained relatively stable. Thus, the two cities are representative examples of different development stages. The distribution patterns of non-impervious and impervious surfaces are also highly heterogeneous in both study areas. Various landcovers such as farmland, aquaculture pond, grassland, mountain vegetation, coastal wetland, and waterbodies were incorporated within the coverage.

Table 1. Main data source.

Location (path/row)	Acquire date	Location (path/row)	Acquire date
Rome, Italy (191/31)	12 August 2013	Shenzhen, Chnia (122/44)	29 November 2013
	21 December 2014		16 November 2014
	17 July 2015		18 October 2015
	19 July 2016		7 February 2016
	6 July 2017		23 October 2017
	25 July 2018		12 February 2018
	26 June 2019		14 November 2019
	30 July 2020		18 February 2020
	11 March 2021		5 December 2021

2.2 Study data and pre-processing

Annual Landsat 8 OLI imageries (path/row: 191/31, 122/44) covering the study areas in Rome and Shenzhen were acquired to form the basic data source (Table 1). In this study, the imageries of Rome were acquired during summer in most of the years, forming a seasonal-consistent dataset. However, the severe cloud coverage substantially affected the accessibility of the cloud-free imageries of Shenzhen. Although we managed to collect the annual dataset of Shenzhen, the imageries were of different seasons. Therefore, it was feasible to evaluate data source limitation and seasonal effect on the proposed method by comparing the results of the two cities. All Landsat 8 OLI imageries were projected into the Transverse Mercator Projection System. The Earth Resources Observation and Science Center of the United States Geological Survey (USGS) performed geometric and radiometric corrections with high accuracy. Atmospheric correction was conducted using Land Surface Reflectance Code (LaSRC). According to the Tasseled Cap Transformation (TCT) wetness component, the waterbody was excluded to reduce misestimation as a pre-processing step. In addition, small plots of QuickBird imageries (resolution: 0.6 m) covering a limited range of the study area in Rome (13 June 2013 and 6 July 2021) and Shenzhen (12 March 2013 and 1 February 2021), were acquired to generate the indispensable sample and validation data (Figure 1).

In order to produce supplementary data, two field surveys were conducted on the impervious surfaces in Rome and Shenzhen city centers in June 2017 and March 2021, respectively. Additionally, two sets of landcover data with a resolution of 30 m, GlobeLand30 and ChinaCover, were also collected as auxiliary data for pixel change detection. GlobeLand30 was developed and published by the Ministry of Natural Resources of China (Jun, Ban, and Songnian 2014). This dataset provides global coverage with high accuracy (Gao et al. 2020). The production of ChinaCover was led by the Institute of Remote Sensing and Digital Earth (RADI) under the Chinese Academy of Sciences (CAS), involving the collaborative efforts of other CAS institutes. Part of the data was edited as an atlas and published by Bingfang (2017).

2.3 Pixel change detection based on remote sensing indicators

The normalized difference impervious surface index (NDISI) and the TCT greenness component were used to detect the pixel's buildup area or vegetation changes. Unlike the normalized differential buildup and bare soil index (NDBSI) or other indexes related to soil or bare lands, NDISI was developed to reduce the mixture of soil and impervious surfaces. As a convenient remote sensing-based indicator, NDISI is closely related to the buildup intensity of the pixels (Hanqiu 2010; Santra et al. 2022). It was calculated using the following equation:

$$NDISI = \frac{\rho_{TIR} - [(MNDWI + \rho_{NIR} + \rho_{SWIR1}/3)]}{\rho_{TIR} + [(MNDWI + \rho_{NIR} + \rho_{SWIR1}/3)]} \quad (1)$$

Where ρ_{NIR},ρ_{SWIR1}, *and* ρ_{TIR} are Landsat 8 OLI imagery's bands 5, 6, and 11. The modified normalized difference water index (MNDWI) can be calculated by the following equation (Hanqiu 2006):

$$MNDWI = \frac{\rho_{green} - \rho_{SWIR1}}{\rho_{green} + \rho_{SWIR1}} \quad (2)$$

Where ρ_{green} and ρ_{SWIR1} are respectively the bands 3 and 6 of Landsat 8 OLI imagery.

Both NDVI and the greenness of TCT are widely used for vegetation monitoring (Xiaoyang et al.

2002). Previous research has indicated that the greenness of TCT can provide additional detail interpretations of vegetation and more sensitive monitoring of the vegetation change compared with NDVI (Samarawickrama, Piyaratne, and Ranagalage 2017; Michael et al. 2016). According to Baig et al. (2014), the TCT greenness component of the Landsat 8 OLI imagery should be calculated as:

$$\begin{aligned} Greenness = &-0.2941\rho_{blue} - 0.243\rho_{green} - 0.5424\rho_{red} \\ &+ 0.7276\rho_{NIR} + 0.0713\rho_{SWIR1} \\ &- 0.1608\rho_{SWIR2} \end{aligned} \quad (3)$$

Where ρ_{blue}, ρ_{green}, ρ_{red}, ρ_{NIR}, ρ_{SWIR1}, and ρ_{SWIR2}, are the corresponding bands 2–7 of the Landsat 8 OLI imagery.

Due to the diversity of landcover distribution in urban areas, most pixels of the medium-resolution imagery are basically mixed by impervious surface, vegetation and soil (Ridd 1995). Therefore, pixel change detection in urban areas should focus on changes related to these key features. This study used these two indicators instead of a conventional single band-based method to improve the detection of the pixel's buildup area or vegetation changes (Song et al. 2001). Previous studies have grouped pixels into ten levels based on normalized remote sensing indicators for further analysis of environmental issues, such as vegetation change and soil erosion (Adilson et al. 2021; Suzuki, Nomaki, and Yasunari 2001; Karaburun 2010). A similar level system was applied in our study. After being normalized, the two indicators were classified into ten levels for each pixel. If one pixel's levels of NDISI and the TCT greenness component both remained unchanged during the entire study period, a changing period was not defined and the pixel was marked as stable (Figure 2a). Otherwise, a period with different levels from the start to the end year was detected as a changing period. Any pixels with two or more changing periods were marked as changing pixels (Figure 2b).

Based on the high-resolution imageries, it is problematic to classify the pixels with only one changing period as either stable or changed (Figure 3). Landcover data (GlobeLand30 for Rome and ChinaCover for Shenzhen) was therefore applied to assist in defining the classes of these pixels. Only two landcover maps at the start and end years were needed to classify these pixels instead of using landcover data for all years of possible change periods. A 3*3 moving window was used to improve the sensibility of the multitemporal change detection.

2.4 Multitemporal estimation of impervious surface

2.4.1 CART

The CART algorithm generates tree models and rule sets to estimate the target variables. The independent variables are recursively partitioned into subsets based on sample data, until the total residual sum

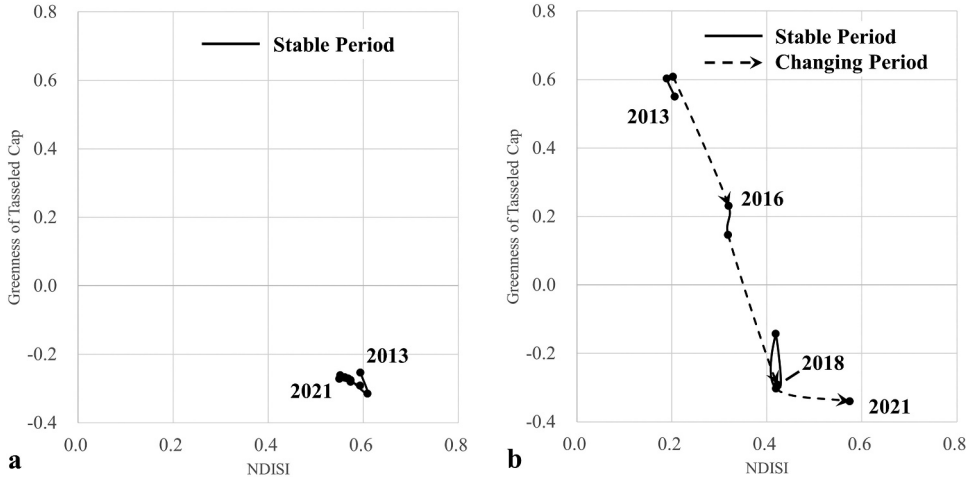

Figure 2. The multitemporal change pathway of NDBSI and TCT greenness component of two typical sample pixels: (a) a stable pixel of intensified buildup area in the east of the Rome study area; and (b) a pixel changed from evergreen broadleaf forest to buildup area in the south of Shenzhen study area. Refer to Figure 1 for the location of the typical sample pixels.

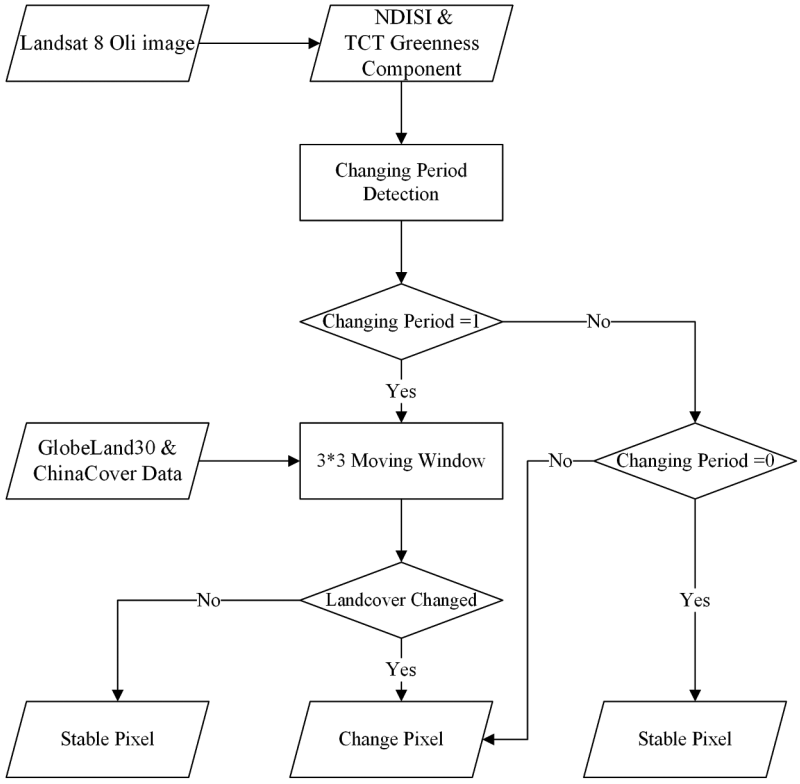

Figure 3. The procedure of pixel change detection based on remote sensing indicators.

square (RSS) of all the subsets is minimized. The kth subset's RSS is determined as follows:

$$RSS_k = \sum_{N_k}^{i=1} (\hat{y} - \bar{y}) \tag{4}$$

where N_k is the quantity of samples in the kth subset, $\hat{y}$ the predicted value of the target variable, and $\bar{y}$ the actual value of the target variable (Breiman et al. 1984). However, based on the above equation, the predicted value ($\hat{y}$) of this algorithm will be the mean value of each subset's actual value ($\bar{y}$), which are single values. Therefore, this algorithm is not able to predict the precise variations within the subsets. Huang and Townshend (2003) employed a linear regression function determined by least square regression to calculate the predicted variables for each subset. Although a linear model may not be globally applicable to the entire dataset, it can be suitable for each subset with normal distributions and little intraclass differences which Breiman's algorithm has effectively classified. Therefore, the complex correlations between percent ISA and spectral reflectance can be theoretically explored by CART.

In this study, eight validation/sample areas were randomly located throughout each study area (Figure 1). Each validation and sample area covered 1.37 km^2, corresponding to 1521 Landsat 8 OLI imagery pixels. Next, 12,168 or half of the pixels in the validation/sample areas were randomly determined to create sample data, while the rest assessed the accuracy. Notably, the validation and sample areas were adequately covered by buildup area and bare lands, which enabled the CART algorithm to distinguish impervious surfaces based on their spectral and spatial features. Object-oriented classification and visual interpretation were then combined to process the high-resolution imageries of 2013 and 2021 for the validation and sample areas, producing binary impervious versus non-impervious maps of the two years. Misclassifications brought by water brink, building and tree shadow, and tiny patch of vegetation were manually modified after visual examination and interpretation. The unchanged areas were defined based on the field survey to enable the pixel in these areas to provide accurate validation and sample data for the entire study period. CART was then applied to estimate the percent ISA in both study

areas. The CART algorithm of this study was created using Cubist, an effective R package tool that can construct tree models with linear regression models in its terminal leaves (http://www.rulequest.com).

2.4.2 Improving impervious surface estimation for stable and changed pixels

Percent ISA was estimated once all pixels in the study area were classified as stable or changed via the method discussed above (Figure 3). The stable pixels' percent ISA remained unchanged from 2013 to 2021 (Figure 2a). Therefore, each stable pixel's percent ISA was calculated by CART based on the spectral reflectance of the imageries throughout the study period. The changing and stable periods had already been defined for each changed pixel. Similar to the stable pixels, the percent ISA in each stable period of the changed pixels should remain unchanged and be estimated using the spectral reflectance of the imageries of the corresponding stable period. The percent ISA for each year in change periods was assigned based on the corresponding imagery's spectral reflectance individually by different CART algorithms.

The compounded errors of conventional CART have been remarkably reduced by the proposed method in this study. Specifically, 10.52% of all pixels in the study areas were defined as stable pixels, and 71.88% were defined as changing pixels with one or more stable periods. Therefore, the percent ISA of these pixels was estimated using the spectral reflectance of at least two Landsat OLI imageries, which substantially reduced the random errors caused by instantaneous imaging conditions. Altogether, the multitemporal percent ISA of 82.40% of the pixels in the study areas was reasonably improved based on change detection.

2.4.3 Accuracy assessment

Throughout each study area, 6084 points were randomly selected to assess the accuracy (Figure 1). In this study, Several error analysis approaches and indicators, such as scatter plot, the residual error (RE), the root-mean-square error (RMSE), and the mean absolute error (MAE), were employed to assess the accuracy of the percent ISA estimation.

The scatter plot is often applied to assess the estimation accuracy in previous impervious studies (Wu and Murray 2003; Xuefei and Weng 2009; Liao et al. 2021; Deng and Zhu 2020; Wang et al. 2018). To form this straightforward accuracy assessment tool, the actual value is placed on one axis and the estimated value on the other. Based on it, the linear fitting function and R^2 can be derived by conventional linear regression.

RE, the discrepancy of the actual and estimated percent ISA is respectively calculated for all the validation pixels. It is calculated by the following equation:

$$RE = \hat{y} - \bar{y} \tag{5}$$

where, $\hat{y}$ and $\bar{y}$ are the estimated and actual percent ISA, respectively.

RMSE and MAE can be derived from the calculation of RE. In existing environmental research, RMSE is one of the most commonly used accuracy assessment indicators. It is derived using the following equation:

$$RMSE = \sqrt{n^{-1}\sum_{n}^{i=1}(\hat{y} - \bar{y})^2} \tag{6}$$

where, n is the number of validation data, $\hat{y}$ and $\bar{y}$ the estimated and actual values. When analyzing errors with RMSE, the values with larger RE have more weight than those with smaller RE. On the contrary, the errors of each validation pixel have equal weight when assessing accuracy using MAE (Chai and Draxler 2014). Therefore, it is regarded as a more explicit and spontaneous indicator than RMSE (Willmott and Matsuura 2005). MAE can be obtained by the following formula:

$$MAE = n^{-1}\sum_{n}^{i=1}|\hat{y} - \bar{y}| \tag{7}$$

where, n indicates number of validation data, $\hat{y}$ and $\bar{y}$ indicate the estimated and actual values, respectively.

3 Results

3.1 Multitemporal percent ISA estimation by the improved method and overall accuracy assessment

Figures 4 and 5 show the impervious surface changes in the two study areas during the study period estimated by the proposed method. Aggregately distributed high-density impervious surfaces are finely delineated, as revealed by the estimated results. At the same time, small plots of low-density (<30%) impervious surfaces and complex-distributed

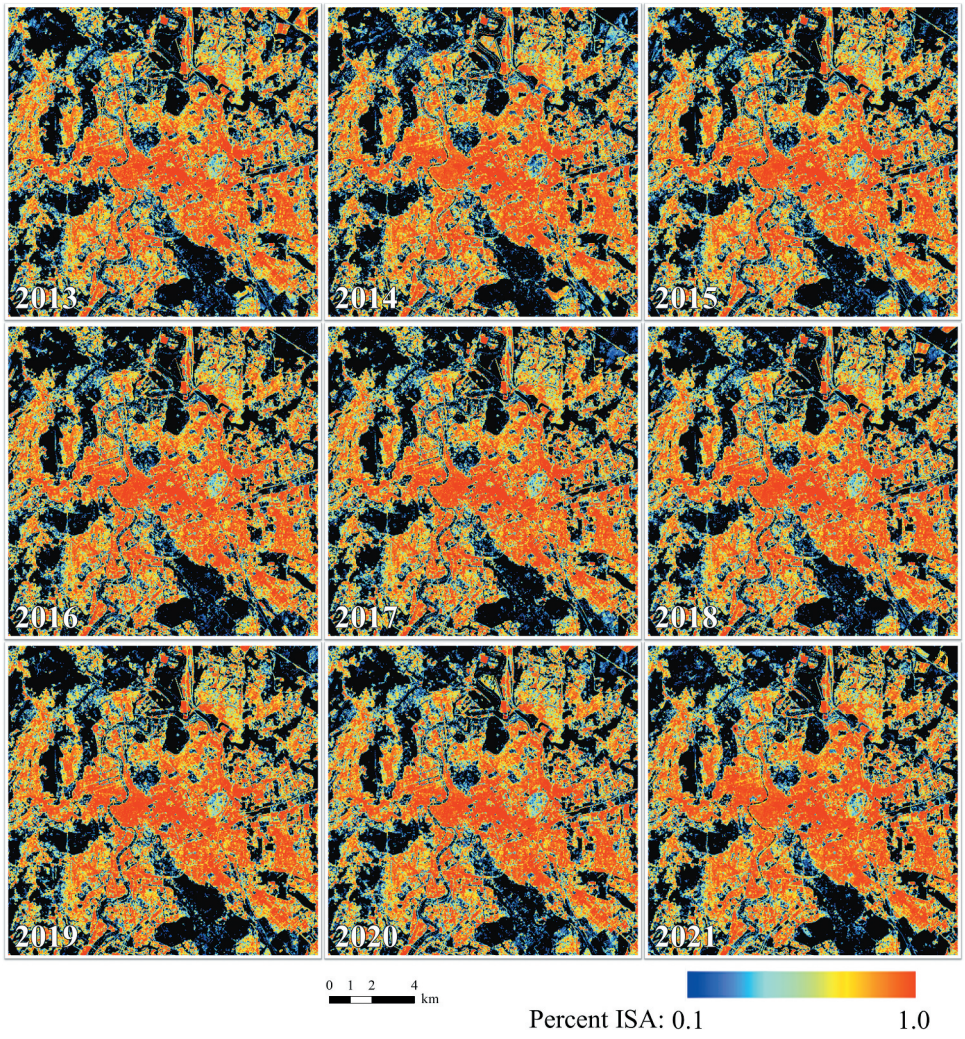

Figure 4. Map of Rome's multitemporal percent ISA (2013–2021) estimated by the improved method.

medium-density (30% – 70%) impervious surfaces were also markedly demonstrated by the estimated results.

The multitemporal changes of the impervious surfaces with different densities are geographically logical and temporally continuous. The distribution of percent ISA in Rome presented typical spatial features of the compact city. The percent ISA varied from high density in the city center to low density in suburban areas, while the percent ISA distributions of Shenzhen indicated a more complex spatial morphology. The high-density impervious surfaces were segmented by large mountain forest areas, forming a multi-center city's spatial feature. In Shenzhen (2021), 73.68% of the pixels were estimated as impervious surfaces with very high density (percent ISA greater than 0.9) or non-impervious surfaces (percent ISA less than 0.1), while this was 51.56% in Rome in 2021. From 2013 to 2021, the distribution and density of impervious surfaces in Rome generally remained stable. Only 0.97% of the study area, covering 2.18 km^2, had a percent ISA increase of more than 0.5 during the study period. These areas were dispersed primarily within the suburban areas. The impervious surfaces of Shenzhen expanded and increased much more remarkably from 2013 to 2021, especially in the northern Shenzhen. It was found that 3.51% of Shenzhen, covering 7.93 km^2, had a percent ISA increase of more than 0.5 during the study period.

Based on the estimated results of percent ISA, this method is able to quantitively analyze the multitemporal change of percent ISA. The mean percent ISA of Rome increased slightly from 0.459 to 0.475 during the study period (Figure 6a). In Shenzhen, a noticeable increase from 0.315 to 0.341 was

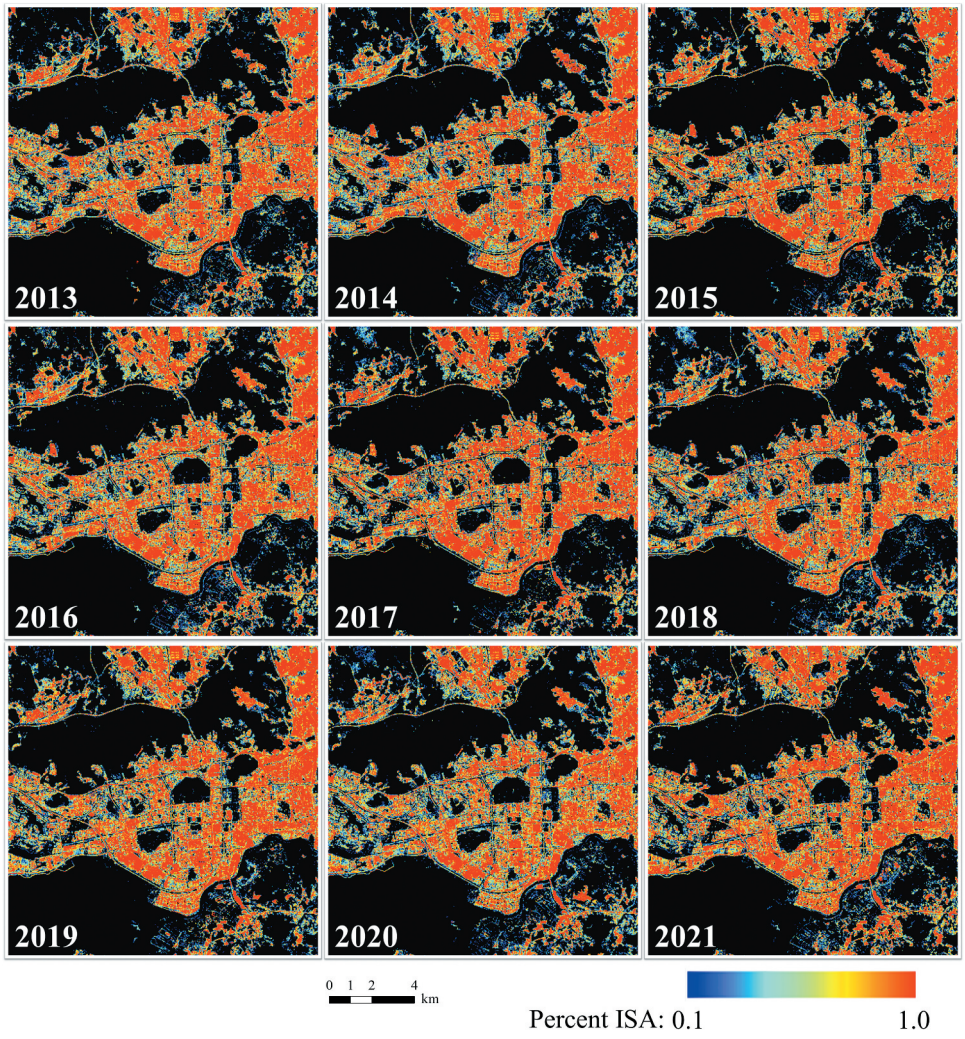

Figure 5. Map of Shenzhen's multitemporal percent ISA (2013–2021) estimated by the improved method.

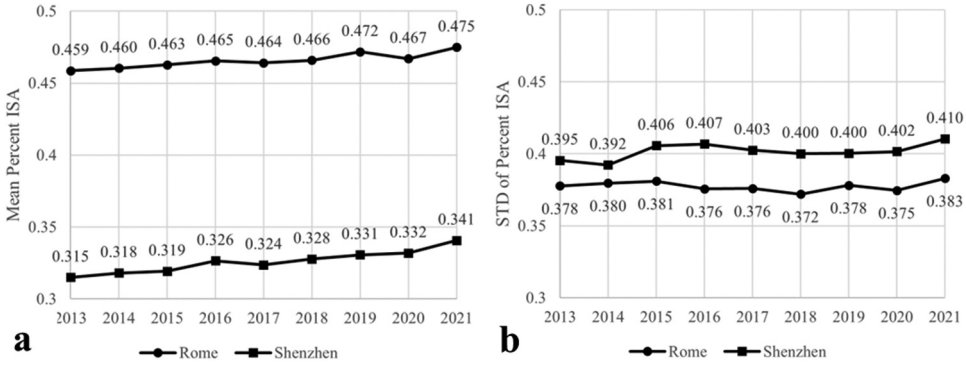

Figure 6. ISA statistics: (a) mean percent ISA; and (b) standard deviation (STD) of percent ISA.

observed. The increasing annual rates of the mean percent ISA recorded in Rome and Shenzhen were 0.44% and 0.99%, respectively. The standard deviation (STD) of percent ISA for Rome and Shenzhen increased from 0.378 to 0.383 and 0.395 to 0.410, respectively. This result demonstrates the growing spatial heterogeneity of the impervious surfaces of both study areas (Figure 6b). The mean percent ISA of Shenzhen was lower at times than that of Rome due to the large water body areas

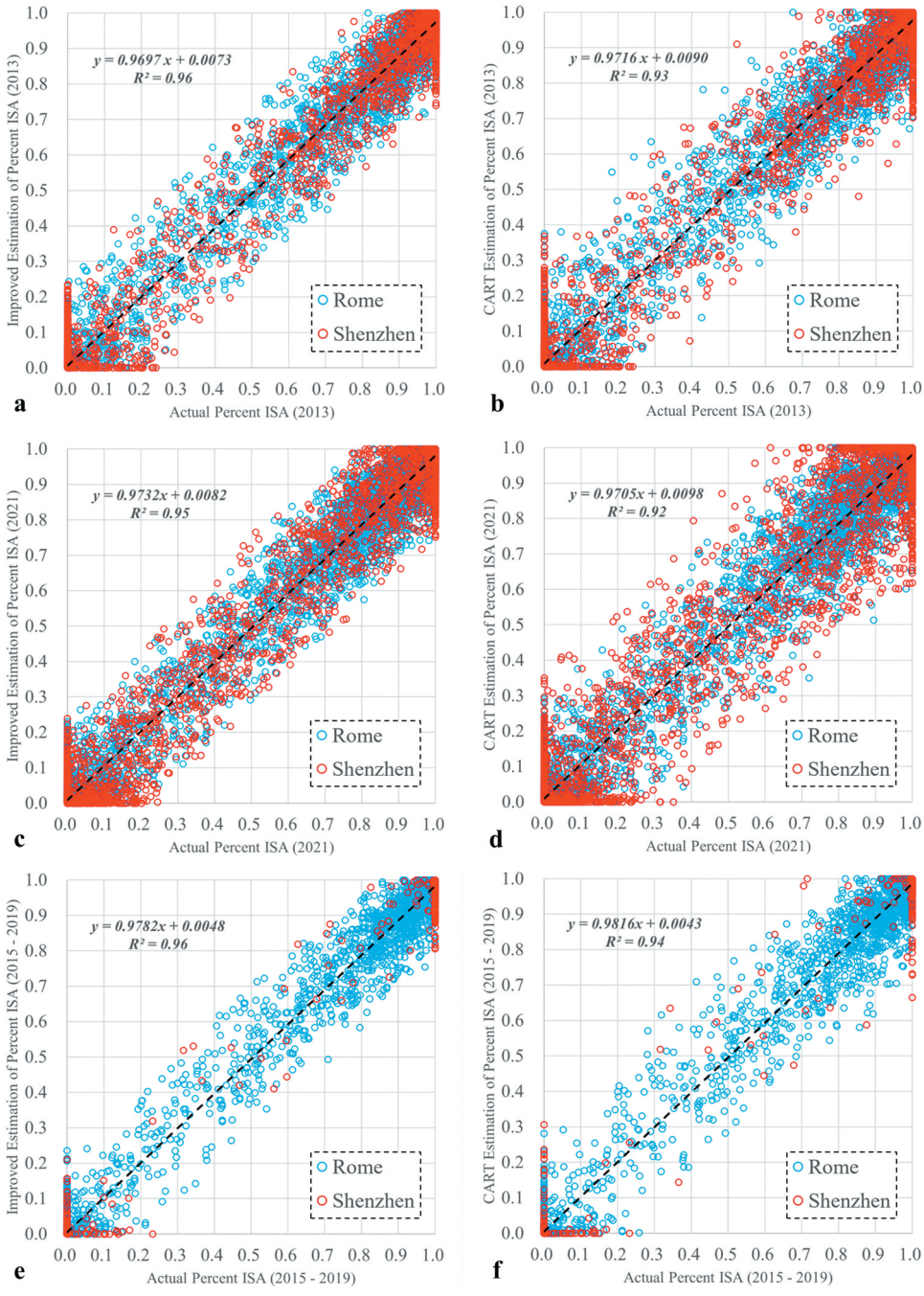

Figure 7. Scatterplots of percent ISA estimation by the improved multitemporal method and conventional CART in 2013 (a and b), 2021 (c and d), and 2015–2019 (e and f) for Rome and Shenzhen.

and mountain vegetation in the city center. However, in Shenzhen, the STD of percent ISA and its increasing speed have both been higher, indicating that the distribution of impervious surfaces in Shenzhen has become increasingly heterogeneous by 2021.

To create comparative results, a conventional CART was conducted based on the same sample datasets for every other year of the studied period. Scatterplots showed the overall accuracy of the estimated percent ISA by the proposed method and conventional CART against actual percent ISA, based on the randomly selected validation data (Figure 7). Both methods gained acceptable accuracy, with a slope approximate to 1 and an intercept close to 0. Compared with conventional CART, the R^2 of the improved method remarkably increased from 0.93 to 0.96 and 0.92 to 0.95, respectively, for the estimation of 2013 (Figure 7 a,b) and 2021 (Figure 7

c,d). Notably, the conventional CART's percent ISA estimation for Shenzhen in 2021 recorded a relatively low R^2. This is likely because of the high heterogeneity of impervious surfaces (Figure 6b). With the proposed multitemporal method, the accuracy of the percent ISA estimation of Shenzhen in 2021 was remarkably improved. Overall, fewer conspicuously misestimated pixels, a higher R^2, and a more optimized fitting curve were observed, in addition to being temporally consistent with the impervious estimation of other years in the study period (Figure 7 a,e).

The stable pixels in the validation areas were defined based on the field survey and the high-resolution imageries acquired in 2013 and 2021. Therefore, these pixels can provide a valid accuracy assessment for percent ISA during the entire study period. There were 5,117 and 4,028 stable pixels in Rome and Shenzhen validation areas, respectively. The stable validation pixels were randomly and equally (approximately) divided into three groups to assess the accuracy of percent ISA estimation in 2015, 2017, and 2019 (Figure 7 e,f). The results demonstrated a noticeable improvement for the proposed method, with R^2 increasing from 0.94 to 0.96, which was similar to the results in 2013 and 2021. It is worth noting that the stable validation pixels in Shenzhen (red point in Figure 7) clustered at both ends of the trend lines. This is because there were more high-density and non-impervious surfaces in Shenzhen compared with Rome, where low/medium-density impervious surfaces were relatively more distributed. This distribution is more remarkable for the validation points of Shenzhen between 2015–2019 (Figure 7 e, f) as only stable pixels, whose percent ISA were more likely to be very high or very low, were used for validating accuracy in this period. Further, the accuracy assessment for the percent ISA estimation in 2015–2019 was not fully sufficient compared with 2013 and 2021 due to the absence of the changing pixels in the validation dataset.

Noticeable improvement can also be confirmed through quantifiable error analysis methods such as MAE and RMSE (Tables 2 and 3). The overall MAE of improved estimation in 2013 and 2021 was reduced by 15.55% and 16.60%, respectively. The overall RMSE of improved estimation in 2013 and 2021 was reduced by 8.63% and 21.28%, respectively. Notably, the improvement is remarkable when the estimation of conventional CART exhibits greater errors. For example, the MAE of the conventional CART's estimation of Rome in 2013 reached the highest value of 4.57. It was reduced to 4.19 with the improved method. The RMSE of the conventional CART's estimation of Shenzhen in 2021 was also relatively high, with the improved method resulting in a decline from 7.04 to 4.98.

3.2 Improvement of stable/changing pixel's percent ISA estimation

In order to quantitively analyze the improvement of the stable pixel's percent ISA estimation by the proposed method, the STD of each stable pixel's multitemporal percent ISA estimation was calculated and statistically analyzed into a boxplot (Figure 8). Ideally, the STD of any stable pixel's multitemporal percent ISA should be 0 because the impervious density has been unchanged during the study period. Notably, the proposed method accurately defined 6,425 (70.26%) of all stable pixels in the validation areas. The boxplot indicated that the proposed method's median, mean, and upper quartile of the STD were lowered by 0.01, 0.01, and 0.02, respectively, compared with the conventional CART.

Table 2. Accuracy comparison of the improved method and conventional CART (2013).

	MAE (%)			RMSE (%)		
	Rome	Shenzhen	Overall	Rome	Shenzhen	Overall
CART	4.57	2.57	3.57	7.24	5.56	6.40
Improved Method	4.19	2.34	3.01	6.52	4.82	5.85

Table 3. Accuracy comparison of the improved method and conventional CART (2021).

	MAE (%)			RMSE (%)		
	Rome	Shenzhen	Overall	Rome	Shenzhen	Overall
CART	4.37	3.06	3.68	7.01	7.04	7.03
Improved Method	3.91	2.32	3.07	6.09	4.98	5.53

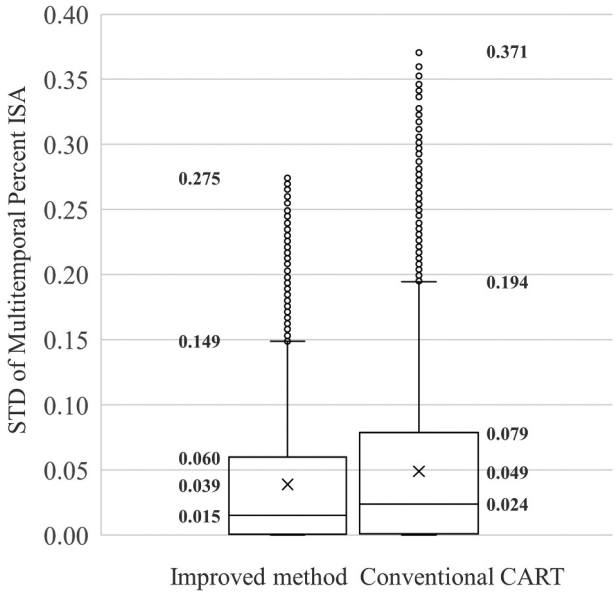

Figure 8. Boxplot showing probability distribution of STD of stable pixel's multitemporal percent ISA estimated by the proposed method and the conventional CART.

Thus, the general improvement of the stable pixels' percent ISA estimation can be confirmed. It is also worth mentioning that the maximum and the most extreme outlier were remarkably reduced by 0.05 and 0.10, respectively, demonstrating the proposed method's conspicuous advantage of correcting the exceedingly misestimated percent ISA.

Table 4 shows the accuracy of percent ISA estimation varying with the number of change periods. MAE and RMSE of pixels without change periods (stable pixels) were both very low, indicating that the improvements of stable pixels' percent ISA estimation were remarkable. Both MAE and RMSE increased with the number of change periods. Notably, the estimation accuracy of the pixels with four or more change periods was very close to that of the conventional CART (Table 3).

Figure 9(a) represents the multitemporal percent ISA of a typical stable pixel with a very high impervious density estimated by the proposed method and conventional CART. The high-resolution imageries demonstrate that the impervious surfaces in this pixel remained completely stable during the study period. However, multitemporal fluctuation of percent ISA that disagreed with the actual earth surface change process still occurred in the CART-estimated results. This false fluctuation of the stable pixels can be observed throughout the study areas, as well as in previous research. Using the proposed improved method, the false fluctuation was profoundly removed for the stable pixels.

Table 4. Accuracy comparison of a different number of change periods (2021).

	Number of Change Periods					
	0	1	2	3	4–8	Overall
MAE (%)	1.89	2.67	2.89	3.41	3.54	3.07
RMSE (%)	3.34	5.33	6.01	6.88	6.99	5.53

Furthermore, the consistency of percent ISA estimation with validation data was also improved for the changed pixel (Figure 9b). The conventional CART algorithm estimated percent ISA with high accuracy in 2021 and prior to 2017. However, it showed a steady increase during the stable period between 2018 and 2020, which was not consistent with the validation data and corresponding high-resolution imageries. In comparison, the stable period of the changed pixel was correctly defined based on the pixel change detection of the proposed method, leading to the accurate multitemporal percent ISA estimation that correlated with the actual earth surface change process.

4 Discussion

In recent years, non-linear models have been continuously implemented to estimate percent ISA with adequate accuracy for a single temporal phase (Jungho et al. 2012; Shao et al. 2015; Feng and Fan 2021). Capable of estimating the non-linear relationship, CART has been widely acknowledged for its outperformance over the linear regression model (Yang et al. 2003; Wang et al. 2018). However, one of the major problems of multitemporal percent ISA estimation using conventional subpixel methods, including CART, is the compounded errors accumulated by each phase's systematic and random errors (Deng and Zhu 2020). The false temporal variations that is in discordance with the actual earth surface change process are discerned from the CART-estimated results in both the current study and previous research (Dengsheng, Moran, and Hetrick 2011; Powell et al. 2007; Wu et al. 2017; Yao et al. 2020).

Higher accuracy in both study areas was achieved without involving extensive auxiliary data and intensive manual tasks. In this study, we required approximately 6,000 sample pixels covering 1.22% of each study area to generate the essential sample data for

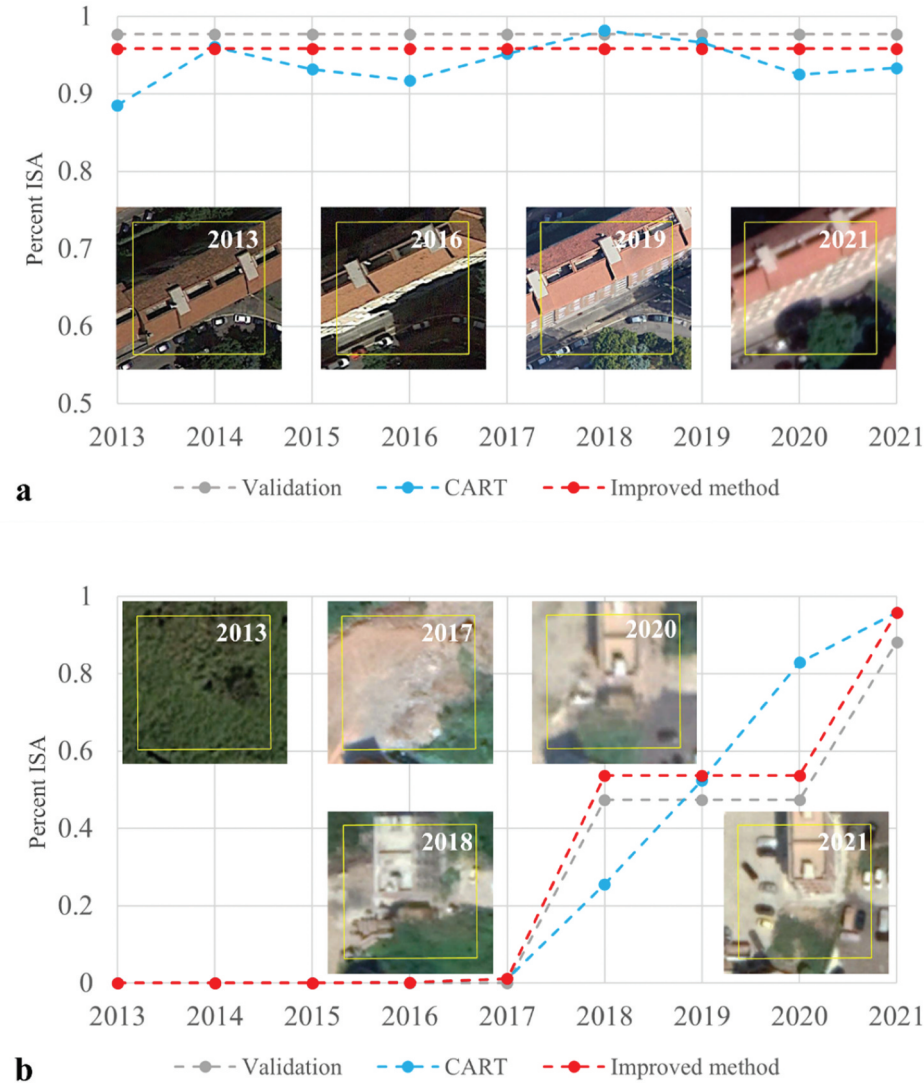

Figure 9. The multitemporal percent ISA change of two typical sample pixels: (a) a stable pixel of intensified buildup area in the east of Rome study area; and (b) a pixel changed from evergreen broadleaf forest to buildup area in the south of the Shenzhen study area. Refer to Figure 1 for the location of the two typical sample pixels and Figure 2 for the spectral change pathway of both pixels.

building the CART algorithm. Moreover, recognizing the unchanged areas makes most of the sample data valid for the entire study period. Hence, sufficient stable sample pixels are accessible even in the study area of Shenzhen, one of the world's most rapidly expanding cities. Therefore, the proposed method can be used globally with much less labored visual interpretation of the high-resolution imageries, which was often conducted individually for each study period in previous research.

Recent research has improved multitemporal percent ISA estimation based on a dense stack of multitemporal cloud-free imageries (Deng and Zhu 2020; Liu et al. 2019). However, this is often not available for coastal cities. In this study, the city of Shenzhen, which is located in the subtropical humid monsoon zone, was selected as a study area. As severe cloud coverage substantially affected data accessibility, only one cloud-free imagery was available for most study years. The season of the imageries acquired for Shenzhen was completely different. Therefore, the proposed method's applicability to estimate percent ISA in areas with poor atmospheric conditions was fully tested. Although imageries in different seasons have been applied to Shenzhen, the accuracy was not lower than in Rome (Tables 2 and Table 3), where a much higher seasonally consistent data source is available. This also shows that the influence of the seasonal effect on the performance of the proposed method shall be negligible. Despite having a substantially lower requirement for cloud-free

Table 5. Accuracy comparison of the proposed method and continuous subpixel monitoring based on CCD.

	MAE %	RMSE %	Number of Imageries	Location	Reference
Random Forest	6.10	12.82	20	Gwadar, Pakistan	Bian et al. (2019)
Continuous subpixel monitoring based on CCD	4.64	7.32	165	Broome County, US	Deng and Zhu (2020)
Proposed method	3.91	6.69	9	Rome, Italy	/

imageries, the proposed method can estimate multitemporal percent ISA with comparable accuracy to the most current method (Table 5).

Shenzhen has experienced a rapid urbanization process over the last ten years, while Rome has remained relatively stable. The historic district of Rome has been covered with impervious surfaces of different densities for thousands of years. In this study, the "eternal" impervious surfaces of the Colosseum with high density and the Roman Forum with low/medium density, and together with surrounding areas were accurately estimated by the proposed method. The changes in ISA in these areas are inconspicuous from 2013 to 2021 (Figure 10). The other study area covers the Futian CBD, Shenzhen, one of China's most prosperous city centers (Figure 11). Built between 2009 and 2017, Ping An International Finance Center is the fourth-tallest supertall skyscraper in the world and China's second-tallest building. The proposed method estimated that the percent ISA of the corresponding pixels increased steadily following the construction of the skyscraper, as well as the south tower and other neighboring buildings. This also shows that the proposed method significantly reduced the errors related to artificial bare lands, which are often mixed with impervious surfaces in linear models (Guiying et al. 2020). This distinguishment is not only based on the slight difference in spectral characteristics of the buildup area and artificial bare lands, but it also relies more on the temporal features. Generally, impervious surfaces are changeless once constructed, while the presence of bare lands is relatively temporary. In Rome and Shenzhen, artificial bare soil changes into impervious surfaces. Thus, pixel change detection in the proposed method could further reduce the mixture problem through temporal features. The precise estimation in the dramatically changing area has proven the proposed method's ability to monitor the actual earth surface change process.

Furthermore, many previous studies estimated multitemporal percent ISA based on the presumption

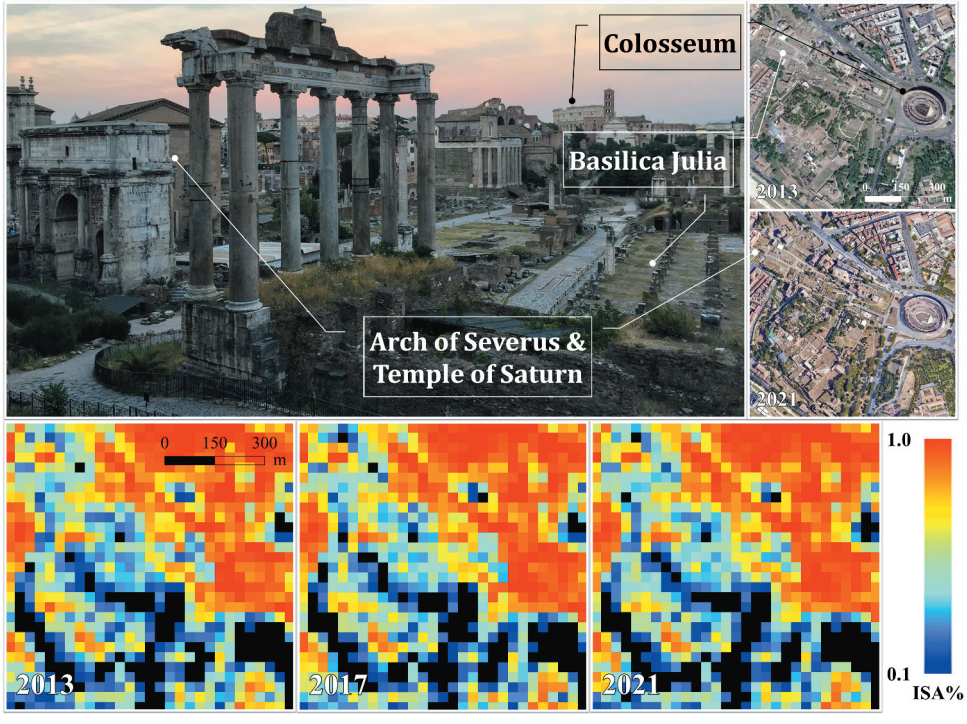

Figure 10. Multitemporal percent ISA estimation for the Colosseum and Roman Forum areas in Rome (photo by Jin Wang in 2017).

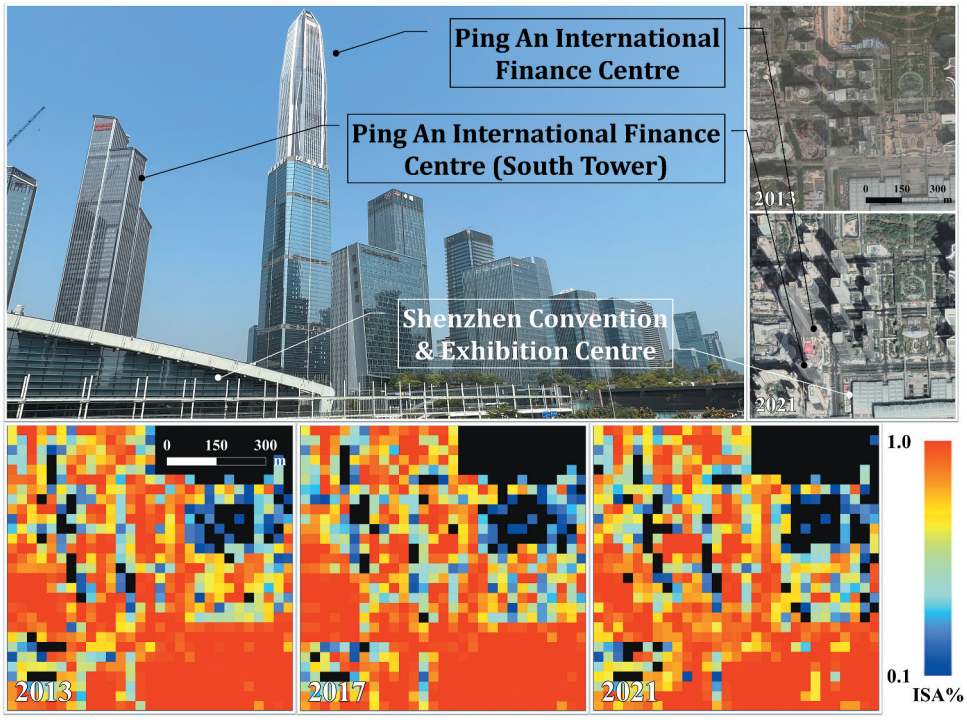

Figure 11. Multitemporal percent ISA estimation in Futian CBD, Shenzhen (photo by Jin Wang in 2021).

that the process of impervious surface expansion and extensification is monodirectional (Song et al. 2016). Direct inter-multitemporal calibration and adjustment of the original estimation results are often involved in producing the final results (Dengsheng, Moran, and Hetrick 2011). However, this assumption may not be universally valid, especially for locations with intensive artificial modification and temporary impervious change (Figure 12). In this study, one of the validation and sample areas in the center of Shenzhen covered many pixels where the buildup area was demolished (Figure 12). Before 2021, the southwestern part of the validation and sample area was the Xiang Mi Hu Holiday Resort, once the largest and the most well-equipped resort in China. However, the resort was demolished, and the land was consolidated to construct the future CBD according to an urban renewal project of the municipal government (Futian District City Renewal and Land Development Bureau), leading to the dramatic decrease in percent ISA for the southwestern part. The proposed method analyses the multitemporal percent ISA based on an objective detection of the pixel's spectral change

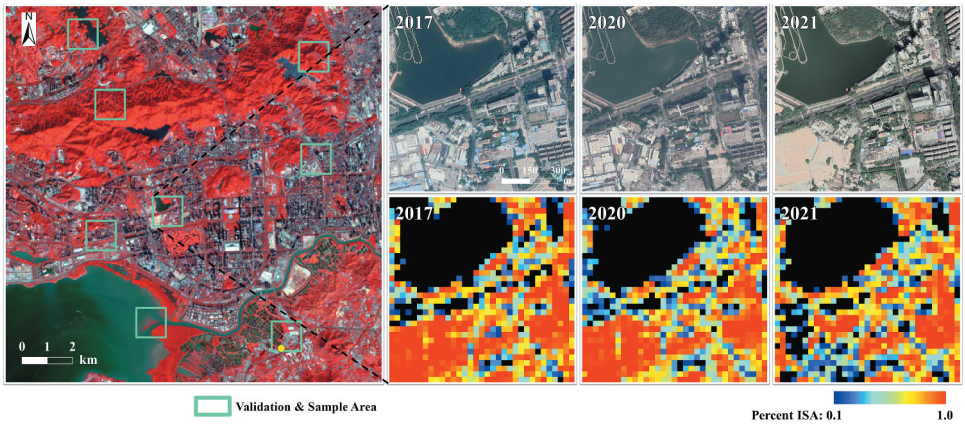

Figure 12. Multitemporal percent ISA estimation of a validation and sample area in Shenzhen. Dramatic percent ISA decrease in the southwestern part occurred with the massive demolition of the buildup area in 2021.

rather than empirical assumptions, thus can authentically record the impervious surface's atypical change. Therefore, the proposed method can be used to monitor the shrinking cities, which has lately gained greater interest.

Another advantage of the proposed method is its high transferability and expansibility. For further improvement, available multi-source data, such as nighttime light imageries, POI data, and RS-based products, can be integrated as supplementary data for pixel change detection. Given that the proposed method requires less mass sample data, optimizing pixel change detection based on multi-source data may also result in improvements. By achieving high accuracy in estimating the variability of impervious surfaces, including historic districts, modern residential areas and contemporary skyscrapers, the proposed method was thoroughly tested by the two study areas. The impervious surfaces of Shenzhen have increased and intensified significantly in the past ten years, which challenges the percent ISA estimation's accuracy. This study also overcomes the data accessibility problem for Shenzhen caused by unfavorable weather conditions. Therefore, the proposed method is transferable to different cities throughout the world.

Notably, cloud-free imageries are unavailable during the entire year for a few cities located in severely rainy areas, such as tropical rainforests. As a result, multitemporal percent ISA estimation of these areas during a relatively long period may have to be conducted based on only a few imageries. Although estimating the stable pixels' percent ISA will not be greatly affected, the estimation of the change pixels' stable periods would be influenced. This is because short-term stable periods would undermine the proposed method's primary advantage in reducing the compounded errors based on multitemporal imageries.

Another limitation of this study may be closely related to the systematic error of the CART algorithm, which often overrates the impervious surfaces with low density and underrates those with high density (Wang et al. 2018; Deng and Zhu 2020). It can decrease the coefficient of x of the fitting curve's function for the accuracy assessment (Figure 7).

5 Conclusion

This study proposed a novel method that improves the multitemporal estimation of percent ISA based on a straightforward pixel change detection approach. The compounded errors of multitemporal estimation were remarkably reduced with a minimum data source and tolerable manual tasks, which prove the proposed method to be objective, reliable, and reproducible. Compared with the conventional method, the overall MAE and RMSE of the proposed method decreased by more than 15.55% and 8.63%, respectively, and R^2 rose from approximately 0.93 to 0.96. The proposed method also remarkably reduced the STD of multitemporal percent ISA of the stable pixels. This method can also be employed to estimate the change of impervious surfaces in shrinking cities or coastal cities with limited remote sensing data sources.

Accurate change estimation of percent ISA has been a challenging research issue for many years due to temporal and spatial complexity. By improving the ISA estimation based on an optimized stable/change pixel detection, reliable fundamental data for environmental research can be accessed. More improvements may occur by further reducing the CART algorithm's systematic error. Other approaches, including intelligent optimizing the sample datasets or deep learning applications to improve the poorly estimated pixels, may be helpful for future studies.

Acknowledgements

We are grateful to Prof. Changshan Wu, University of Wisconsin-Milwaukee for commenting and titling the manuscript. This work was supported by the National Natural Science Foundation of China (No. 42001365, 42001286), the Fundamental Research Foundation of Shenzhen Technology and Innovation Council (Project No. KCXFZ202002011006298).

Disclosure statement

No potential conflict of interest was reported by the author(s).

Funding

This work was supported by the National Natural Science Foundation of China [42001286]; National Natural Science Foundation of China [42001365]; Fundamental Research Foundation of Shenzhen Technology and Innovation Council [KCXFZ202002011006298].

ORCID

Wei Fan http://orcid.org/0000-0002-0508-523X
Paolo Tarolli http://orcid.org/0000-0003-0043-5226
Jin Wang http://orcid.org/0000-0003-2584-9644

Data availability statement

The medium-resolution remote sensing imagery used for this study can be acquired via USGS (https://earthexplorer.usgs.gov). GlobeLand30 product as ancillary land census data can be acquired via the official website run by the Ministry of Natural Resources of China (http://www.globallandcover.com/home_en.html).

References

Adilson, B., N. N. Imai, L. E. Christovam, M. L. B. T. Galo, A. M. G. Tommaselli, and E. Honkavaara. 2021. "Analysis of Trends and Changes in the Successional Trajectories of Tropical Forest Using the Landsat NDVI Time Series." *Remote Sensing Applications: Society and Environment* 24: 100622. doi:10.1016/j.rsase.2021.100622.

Arnold, C. L.,sJr, and C. James Gibbons. 1996. "Impervious Surface Coverage: The Emergence of a Key Environmental Indicator." *Journal of the American Planning Association* 62 (2): 243–258. doi:10.1080/01944369608975688.

Baig, M. H. A., L. Zhang, T. Shuai, and Q. Tong. 2014. "Derivation of a Tasselled Cap Transformation Based on Landsat 8 at-satellite Reflectance." *Remote Sensing Letters* 5 (5): 423–431. doi:10.1080/2150704X.2014.915434.

Bauer, M. E., N. J. Heinert, J. K. Doyle, and F. Yuan. 2004. Impervious Surface Mapping and Change Monitoring Using Landsat Remote Sensing. Paper presented at the ASPRS annual conference proceedings, Denver, Colorado.

Bian, J., L. Ainong, J. Zuo, G. Lei, Z. Zhang, and X. Nan. 2019. "Estimating 2009–2017 Impervious Surface Change in Gwadar, Pakistan Using the HJ-1A/B Constellation, GF-1/2 Data, and the Random Forest Algorithm." *ISPRS International Journal of Geo-Information* 8 (10): 443. doi:10.3390/ijgi8100443.

Bingfang, W. 2017. *Land Cover Atlas of the People's Republic of China (1:1000000)*. Beijing, China: SinoMaps Press.

Breiman, L. I., J. H. Friedman, R. A. Olshen, and C. J. Stone. 1984. "Classification and Regression Trees (CART)." *Encyclopedia of Ecology* 40 (3): 358.

Cablk, M. E., and T. B. Minor. 2003. "Detecting and Discriminating Impervious Cover with high-resolution IKONOS Data Using Principal Component Analysis and Morphological Operators." *International Journal of Remote Sensing* 24 (23): 4627–4645. doi:10.1080/0143116031000102539.

Cao, S., H. Deyong, W. Zhao, M. You, Y. Chen, and Y. Zhang. 2019. "Monitoring Changes in the Impervious Surfaces of Urban Functional Zones Using multi-source Remote Sensing Data: A Case Study of Tianjin, China." *GIScience & Remote Sensing* 56 (7): 967–987. doi:10.1080/15481603.2019.1600110.

Chai, T., and R. R. Draxler. 2014. "Root Mean Square Error (RMSE) or Mean Absolute Error (Mae)?–arguments against Avoiding RMSE in the Literature." *Geoscientific Model Development* 7 (3): 1247–1250. doi:10.5194/gmd-7-1247-2014.

Chen, R., L. Xiaodong, Y. Zhang, P. Zhou, Y. Wang, L. Shi, L. Jiang, F. Ling, and D. Yun. 2021. "Spatiotemporal Continuous Impervious Surface Mapping by Fusion of Landsat Time Series Data and Google Earth Imagery." *Remote Sensing* 13 (12): 2409. doi:10.3390/rs13122409.

Dams, J., J. Dujardin, R. Reggers, I. Bashir, F. Canters, and O. Batelaan. 2013. "Mapping Impervious Surface Change from Remote Sensing for Hydrological Modeling." *Journal of Hydrology* 485 (485): 84–95. doi:10.1016/j.jhydrol.2012.09.045.

Deng, C., and Z. Zhu. 2020. "Continuous Subpixel Monitoring of Urban Impervious Surface Using Landsat Time Series." *Remote Sensing of Environment* 238: 110929. doi:10.1016/j.rse.2018.10.011.

Dengsheng, L., E. Moran, and S. Hetrick. 2011. "Detection of Impervious Surface Change with Multitemporal Landsat Images in an urban–rural Frontier." *ISPRS Journal of Photogrammetry and Remote Sensing* 66 (3): 298–306. doi:10.1016/j.isprsjprs.2010.10.010.

Dipanwita, D., S. K. P. Atiqur Rahman, A. Kundu. 2021. "Impervious Surface Growth and Its inter-relationship with Vegetation Cover and Land Surface Temperature in peri-urban Areas of Delhi." *Urban Climate* 37: 100799. doi:10.1016/j.uclim.2021.100799.

Dougherty, M., R. L. Dymond, S. J. Goetz, C. A. Jantz, and N. Goulet. 2004. "Evaluation of Impervious Surface Estimates in a Rapidly Urbanizing Watershed." *Photogrammetric Engineering & Remote Sensing* 70 (11): 1275–1284. doi:10.14358/PERS.70.11.1275.

Duran, Z., Musaoglu, N., Seker, D. Z. 2006."Evaluating urban land use change in historical peninsula, Istanbul, by using GIS and remote sensing." *Fresenius Environmental Bulletin* 15: 1018-4619.

Feng, S., and F. Fan. 2021. "Impervious Surface Extraction Based on Different Methods from Multiple Spatial Resolution Images: A Comprehensive Comparison." *International Journal of Digital Earth* 14 (9): 1148–1174. doi:10.1080/17538947.2021.1936227.

Futian District City Renewal and Land Development Bureau. "Urban Renewal Unit Plan of Xiang Mi Hu Holiday Resort, Xiang Mi Hu Sub-district, Futian District, Shenzhen." http://www.sz.gov.cn/szzt2010/wgkzl/jcgk/jcygk/zdzcjc/content/post_9259551.html.

Gao, Y., L. Liu, X. Zhang, X. Chen, M. Jun, and S. Xie. 2020. "Consistency Analysis and Accuracy Assessment of Three Global 30-m land-cover Products over the European Union Using the LUCAS Dataset." *Remote Sensing* 12 (21): 3479. doi:10.3390/rs12213479.

Guiying, L., L. Longwei, L. Dengsheng, W. Guo, and W. Kuang. 2020. "Mapping Impervious Surface Distribution in China Using multi-source Remotely Sensed Data." *Giscience &*

Remote Sensing 57 (4): 543–552. doi:10.1080/15481603.2020.1744240.

Hanqiu, X. 2006. "Modification of Normalised Difference Water Index (NDWI) to Enhance Open Water Features in Remotely Sensed Imagery." *International Journal of Remote Sensing* 27 (14): 3025–3033. doi:10.1080/01431160600589179.

Hanqiu, X. 2010. "Analysis of Impervious Surface and Its Impact on Urban Heat Environment Using the Normalized Difference Impervious Surface Index (NDISI)." *Photogrammetric Engineering & Remote Sensing* 76 (5): 557–565. doi:10.14358/PERS.76.5.557.

Hsieh, P. F., L. C. Lee, and N. Yu Chen. 2001. "Effect of Spatial Resolution on Classification Errors of Pure and Mixed Pixels in Remote Sensing." *Geoscience and Remote Sensing, IEEE Transactions on* 39 (12): 2657–2663. doi:10.1109/36.975000.

Huafei, Y., Y. Zhao, F. Yingchun, and L. Li. 2018. "Spatiotemporal Variance Assessment of Urban Rainstorm Waterlogging Affected by Impervious Surface Expansion: A Case Study of Guangzhou, China." *Sustainability* 10 (10): 3761. doi:10.3390/su10103761.

Huang, M., N. Chen, D. Wenying, M. Wen, D. Zhu, and J. Gong. 2021. "An on-demand Scheme Driven by the Knowledge of Geospatial Distribution for large-scale high-resolution Impervious Surface Mapping." *Giscience & Remote Sensing* 58 (4): 562–586. doi:10.1080/15481603.2021.1909304.

Huang, C., and J. R. G. Townshend. 2003. "A Stepwise Regression Tree for Nonlinear Approximation: Applications to Estimating Subpixel Land Cover." *International Journal of Remote Sensing* 24 (1): 75–90. doi:10.1080/01431160305001.

Huidong, L., Y. Zhou, G. Jia, K. Zhao, and J. Dong. 2022. "Quantifying the Response of Surface Urban Heat Island to Urbanization Using the Annual Temperature Cycle Model." *Geoscience Frontiers* 13 (1): 101141. doi:10.1016/j.gsf.2021.101141.

ISTAT, Italian National Institute of Statistics. 2021. "Resident Population on 1st January: Roma Province." In.

Jiaqiang, D., F. Qing, S. Fang, W. Jinhua, H. Ping, and Z. Quan. 2019. "Effects of Rapid Urbanization on Vegetation Cover in the Metropolises of China over the Last Four Decades." *Ecological Indicators* 107: 105458. doi:10.1016/j.ecolind.2019.105458.

Jun, C., Y. Ban, and L. Songnian. 2014. "Open Access to Earth land-cover Map." *Nature* 514 (7523): 434. doi:10.1038/514434c.

Jungho, I., L. Zhenyu, J. Rhee, and L. J. Quackenbush. 2012. "Impervious Surface Quantification Using a Synthesis of Artificial Immune Networks and decision/regression Trees from multi-sensor Data." *Remote Sensing of Environment* 117: 102–113. doi:10.1016/j.rse.2011.06.024.

Karaburun, A. 2010. "Estimation of C Factor for Soil Erosion Modeling Using NDVI in Buyukcekmece Watershed." *Ozean Journal of Applied Sciences* 3 (1): 77–85.

Lamar, W. R., J. B. McGraw, and T. A. Warner. 2005. "Multitemporal Censusing of a Population of Eastern Hemlock (Tsuga Canadensis L.) from Remotely Sensed Imagery Using an Automated Segmentation and Reconciliation Procedure." *Remote Sensing of Environment* 94 (1): 133–143. doi:10.1016/j.rse.2004.09.003.

Liao, W., Y. Deng, L. Miao, M. Sun, J. Yang, and X. Jianhui. 2021. "Extraction and Analysis of Finer Impervious Surface Classes in Urban Area." *Remote Sensing* 13 (3): 459. doi:10.3390/rs13030459.

Limin, Y., G. Xian, J. M. Klaver, and B. Deal. 2003. "Urban Land-Cover Change Detection through Sub-Pixel Imperviousness Mapping Using Remotely Sensed Data." *Photogrammetric Engineering & Remote Sensing* 69 (9): 1003–1010. doi:10.14358/PERS.69.9.1003.

Liu, C., Q. Zhang, H. Luo, Q. Shuhua, S. Tao, X. Hanzeyu, and Y. Yao. 2019. "An Efficient Approach to Capture Continuous Impervious Surface Dynamics Using spatial-temporal Rules and Dense Landsat Time Series Stacks." *Remote Sensing of Environment* 229: 114–132. doi:10.1016/j.rse.2019.04.025.

Luo, Y., Y. Zhao, K. Yang, K. Chen, M. Pan, and X. Zhou. 2018. "Dianchi Lake Watershed Impervious Surface Area Dynamics and Their Impact on Lake Water Quality from 1988 to 2017." *Environmental Science and Pollution Research* 25 (29): 29643–29653. doi:10.1007/s11356-018-2967-1.

Mathew, A., S. Khandelwal, and N. Kaul. 2016. "Spatial and Temporal Variations of Urban Heat Island Effect and the Effect of Percentage Impervious Surface Area and Elevation on Land Surface Temperature: Study of Chandigarh City, India." *Sustainable Cities and Society* 26: 264–277. doi:10.1016/j.scs.2016.06.018.

Michael, S., J. G. P. W. Clevers, S. Carter, J. Verbesselt, V. Avitabile, H. Vu Quang, and M. Herold. 2016. "Performance of Vegetation Indices from Landsat Time Series in Deforestation Monitoring." *International Journal of Applied Earth Observation and Geoinformation* 52: 318–327. doi:10.1016/j.jag.2016.06.020.

Phinn, S., M. Stanford, P. Scarth, A. T. Murray, and P. T. Shyy. 2002. "Monitoring the Composition of Urban Environments Based on the vegetation-impervious surface-soil (VIS) Model by Subpixel Analysis Techniques." *International Journal of Remote Sensing* 23 (20): 4131–4153. doi:10.1080/01431160110114998.

Pilon, P. G. 1988. "An Enhanced Classification Approach to Change Detection in semi-arid Environments." *Photogramm. Eng. Remote Sens* 54: 1709–1716.

Piyoosh, A. K., and S. Kumar Ghosh. 2017. "Semi-automatic Mapping of Anthropogenic Impervious Surfaces in an urban/suburban Area Using Landsat 8 Satellite Data." *GIScience & Remote Sensing* 54 (4): 471–494. doi:10.1080/15481603.2017.1282414.

Powell, R. L., D. A. Roberts, P. E. Dennison, and L. L. Hess. 2007. "Sub-pixel Mapping of Urban Land Cover Using Multiple Endmember Spectral Mixture Analysis: Manaus, Brazil." *Remote Sensing of Environment* 106 (2): 253–267. doi:10.1016/j.rse.2006.09.005.

Ridd, M. K. 1995. "Exploring a VIS (vegetation-impervious surface-soil) Model for Urban Ecosystem Analysis through Remote Sensing: Comparative Anatomy for Cities." *International Journal of Remote Sensing* 16 (12): 2165–2185. doi:10.1080/01431169508954549.

Salerno, F., V. Gaetano, and T. Gianni. 2018. "Urbanization and Climate Change Impacts on Surface Water Quality:

Enhancing the Resilience by Reducing Impervious Surfaces." *Water Research* 144: 491–502. doi:10.1016/j.watres.2018.07.058.

Samarawickrama, U., D. Piyaratne, and M. Ranagalage. 2017. "Relationship between NDVI with Tasseled Cap Indices: A Remote Sensing Based Analysis." *International Journal of Innovative Research in Technology* 3 (12): 13–19.

Santra, A., A. Kumar, S. S. Mitra, and D. Mitra. 2022. "Identification of Built-Up Areas Based on the Consistently High Heat-Radiating Surface in the Kolkata Metropolitan Area." *Journal of the Indian Society of Remote Sensing* 50: 1–15.

Schueler, T. R. 1994. "The Importance of Imperviousness." *Watershed Protection Techniques* 1 (3): 100–111.

Sekertekin, A., and E. Zadbagher. 2021. "Simulation of Future Land Surface Temperature Distribution and Evaluating Surface Urban Heat Island Based on Impervious Surface Area." *Ecological Indicators* 122: 107230. doi:10.1016/j.ecolind.2020.107230.

Shao, Y., G. L. Li, E. Guenther, and J. B. Campbell. 2015. "Evaluation of Topographic Correction on Subpixel Impervious Cover Mapping with CBERS-2B Data." *IEEE Geoscience and Remote Sensing Letters* 12 (8): 1675–1679. doi:10.1109/LGRS.2015.2419135.

Shao, Z., and C. Liu. 2014. "The Integrated Use of DMSP-OLS Nighttime Light and MODIS Data for Monitoring large-scale Impervious Surface Dynamics: A Case Study in the Yangtze River Delta." *Remote Sensing* 6 (10): 9359–9378. doi:10.3390/rs6109359.

Shenzhen Statistics Bureau. 2021. "Communiqué of the Seventh National Population Census (Shenzhen)." 1: 1.

Sinha, S., A. Santra, and S. Santra Mitra. 2020. "Semi-automated Impervious Feature Extraction Using built-up Indices Developed from space-borne Optical and SAR Remotely Sensed Sensors." *Advances in Space Research* 66 (6): 1372–1385. doi:10.1016/j.asr.2020.05.040.

Song, X.-P., J. O. Sexton, C. Huang, S. Channan, and J. R. Townshend. 2016. "Characterizing the Magnitude, Timing and Duration of Urban Growth from Time Series of Landsat-based Estimates of Impervious Cover." *Remote Sensing of Environment* 175: 1–13. doi:10.1016/j.rse.2015.12.027.

Song, C., C. E. Woodcock, K. C. Seto, M. Pax Lenney, and S. A. Macomber. 2001. "Classification and Change Detection Using Landsat TM Data: When and How to Correct Atmospheric Effects?" *Remote Sensing of Environment* 75 (2): 230–244. doi:10.1016/S0034-4257(00)00169-3.

Stow D. A., and Chen, D. Mei. 2002. "Sensitivity of multitemporal NOAA AVHRR data of an urbanizing region to land-use/land-cover changes and misregistration." *Remote Sensing of Environment* 80 (2): 297–307. doi:10.1016/S0034-4257(01)00311-X

Suzuki, R., T. Nomaki, and T. Yasunari. 2001. "Spatial Distribution and Its Seasonality of Satellite-derived Vegetation Index (NDVI) and Climate in Siberia." *International Journal of Climatology: A Journal of the Royal Meteorological Society* 21 (11): 1321–1335. doi:10.1002/joc.653.

UNHabitat 2016. "World Cities Report 2016: Urbanization and Development - Emerging Futures."

UNHabitat 2020. "World Cities Report 2020."

Wang, Y., and L. Mingshi. 2021. "Urban Impervious Surface Automatic Threshold Detection Model Derived from Multitemporal Landsat Images." *IEEE Transactions on Geoscience and Remote Sensing* 60: 1–21.

Wang, J., W. Zhifeng, W. Changshan, Z. Cao, W. Fan, and P. Tarolli. 2018. "Improving Impervious Surface Estimation: An Integrated Method of Classification and Regression Trees (CART) and Linear Spectral Mixture Analysis (LSMA) Based on Error Analysis." *GIScience & Remote Sensing* 55 (4): 583–603. doi:10.1080/15481603.2017.1417690.

Weng, Q. 2012. "Remote Sensing of Impervious Surfaces in the Urban Areas: Requirements, Methods, and Trends." *Remote Sensing of Environment* 117: 34–49. doi:10.1016/j.rse.2011.02.030.

Willmott, C. J., and K. Matsuura. 2005. "Advantages of the Mean Absolute Error (MAE) over the Root Mean Square Error (RMSE) in Assessing Average Model Performance." *Climate Research* 30 (1): 79–82. doi:10.3354/cr030079.

Wu, C. 2004."Normalized spectral mixture analysis for monitoring urban composition using ETM+ imagery." *Remote Sensing of Environment* 93 (4): 480–492. doi:10.1016/j.rse.2004.08.003

Wu, C., and A. T. Murray. 2003. "Estimating Impervious Surface Distribution by Spectral Mixture Analysis." *Remote Sensing of Environment* 84 (4): 493–505. doi:10.1016/S0034-4257(02)00136-0.

Wu, K., D. Qian, Y. Wang, and Y. Yang. 2017. "Supervised sub-pixel Mapping for Change Detection from Remotely Sensed Images with Different Resolutions." *Remote Sensing* 9 (3): 284. doi:10.3390/rs9030284.

Xian, G., and M. Crane. 2005. "Assessments of Urban Growth in the Tampa Bay Watershed Using Remote Sensing Data." *Remote Sensing of Environment* 97 (2): 203–215. doi:10.1016/j.rse.2005.04.017.

Xian, G., and C. Homer. 2010. "Updating the 2001 National Land Cover Database Impervious Surface Products to 2006 Using Landsat Imagery Change Detection Methods." *Remote Sensing of Environment* 114 (8): 1676–1686. doi:10.1016/j.rse.2010.02.018.

Xiaoyang, Z., C. Barker Schaaf, M. A. Friedl, A. H. Strahler, F. Gao, and J. C. F. Hodges. 2002. MODIS Tasseled Cap Transformation and Its Utility. Paper presented at the IEEE International Geoscience and Remote Sensing Symposium, Toronto, Canada.

Xuefei, H., and Q. Weng. 2009. "Estimating Impervious Surfaces from Medium Spatial Resolution Imagery Using the self-organizing Map and multi-layer Perceptron Neural Networks." *Remote Sensing of Environment* 113 (10): 2089–2102. doi:10.1016/j.rse.2009.05.014.

Yang, L., C. Huang, C. G. Homer, B. K. Wylie, and M. J. Coan. 2003. "An Approach for Mapping large-area Impervious Surfaces: Synergistic Use of Landsat-7 ETM+ and High Spatial Resolution Imagery." *Canadian Journal of Remote Sensing* 29 (2): 230–240. doi:10.5589/m02-098.

Yang, L., L. Jiang, H. Lin, and M. Liao. 2009. "Quantifying sub-pixel Urban Impervious Surface through Fusion of Optical and InSAR Imagery." *GIScience & Remote Sensing* 46 (2): 161–171. doi:10.2747/1548-1603.46.2.161.

Yao, N., C. Huang, J. Yang, C. C. Konijnendijk van den Bosch, M. Lvyi, and Z. Jia. 2020. "Combined Effects of Impervious Surface Change and large-scale Afforestation on the Surface Urban Heat Island Intensity of Beijing, China Based on Remote Sensing Analysis." *Remote Sensing* 12 (23): 3906. doi:10.3390/rs12233906.

Yuan, F., and M. E. Bauer. 2007. "Comparison of Impervious Surface Area and Normalized Difference Vegetation Index as Indicators of Surface Urban Heat Island Effects in Landsat Imagery." *Remote Sensing of Environment* 106 (3): 375–386. doi:10.1016/j.rse.2006.09.003.

Zhang, Y., H. Zhang, and H. Lin. 2014. "Improving the Impervious Surface Estimation with Combined Use of Optical and SAR Remote Sensing Images." *Remote Sensing of Environment* 141: 155–167. doi:10.1016/j.rse.2013.10.028.

Zhu, Z. 2017. "Change Detection Using Landsat Time Series: A Review of Frequencies, pre-processing, Algorithms, and Applications." *ISPRS Journal of Photogrammetry and Remote Sensing* 130: 370–384. doi:10.1016/j.isprsjprs.2017.06.013.